

17 Abstract

18 The Bering Sea is one of the most biologically productive regions in the marine system and plays
19 a key role in regulating the flow of waters to the Arctic Ocean and into the subarctic North
20 Pacific Ocean. Cores from IODP Expedition 323 to the Bering Sea provide the first opportunity
21 to obtain reconstructions from the region that extend back to the Pliocene. Previous research at
22 Bowers Ridge, south Bering Sea, has revealed stable levels of siliceous productivity over the
23 onset of major Northern Hemisphere Glaciation (NHG) (c. 2.85-2.73 Ma). However, diatom
24 silica isotope records of oxygen ($\delta^{18}\text{O}_{\text{diatom}}$) and silicon ($\delta^{30}\text{Si}_{\text{diatom}}$) presented here demonstrate
25 that this interval was associated with a progressive increase in the supply of silicic acid to the
26 region, superimposed on shift to a more dynamic environment characterized by colder
27 temperatures and increased sea ice. This concluded at 2.58 Ma with a sharp increase in diatom
28 productivity, further increases in photic zone nutrient availability and a permanent shift to colder
29 sea surface conditions. These transitions are suggested to reflect a gradually more intense
30 nutrient leakage from the subarctic northwest Pacific Ocean, with increases in productivity
31 further aided by increased sea-ice and wind-driven mixing in the Bering Sea. In suggesting a
32 linkage in biogeochemical cycling between the south Bering Sea and subarctic Northwest Pacific
33 Ocean, mainly via the Kamchatka Strait, this work highlights the need to consider the inter-
34 connectivity of these two systems when future reconstructions are carried out in the region.

35 1 Introduction

36 The progressive advancement of ice sheets across the Northern Hemisphere in the late
37 Pliocene and the development of glacial-interglacial cycles which punctuate the Quaternary mark
38 a significant threshold in Earth's climate history [Ravelo et al., 2004]. Of particular note are the
39 transitions associated with the onset of major Northern Hemisphere Glaciation (NHG), c. 2.85-
40 2.73 Ma, when large ice sheets developed across Greenland, Eurasia and Northern America
41 [Raymo 1994; Maslin et al., 1996; Hidy et al., 2013]. Investigating the changes that occurred
42 over this time-frame is important for understanding the long-term functionality and temporal
43 variability of the global climate system [Mudelsee and Raymo, 2005]. Until recently the paucity
44 of cores from the Bering Sea prevented a reconstruction of regional oceanographic conditions
45 beyond the last glacial cycle. The absence of such records is notable given the sea is one of the
46 most highly productive high-nutrient low-chlorophyll (HNLC) marine systems [Sambrotto et al.,
47 1984; Brown et al., 2011]. For the first time, cores from IODP Expedition 323 allow the history
48 of the Bering Sea to be reconstructed over the Pliocene/Quaternary interval with Site U1341,
49 situated on the western flank of Bowers Ridge south of the modern sea ice extent (Fig. 1),
50 permitting an examination of how conditions are interlinked with the wider North Pacific region
51 [Takahashi et al., 2011; Kinney and Maslowski, 2012].

52 Prior to IODP Expedition 323, knowledge of the long-term behavior of the wider
53 subarctic region was primarily restricted to reconstructions from ODP Site 882 in the subarctic
54 Northwest Pacific Ocean which show a major restructuring of oceanographic conditions over the
55 onset of NHG (Fig. 1). Throughout the mid-Pliocene records from ODP Site 882 indicate a
56 mixed water column characterized by high opal mass accumulation rates (MAR) (c. $3 \text{ g cm}^{-2} \text{ ka}^{-1}$),
57 conditions that would have helped maintain a warm climate state via significant deep water
58 upwelling and ventilation of CO_2 to the atmosphere [Haug et al., 1999; Haug et al., 2005]. After
59 2.73 Ma increases in surface freshwater led to the formation of a halocline that initiated a
60 collapse in siliceous productivity (opal MAR = $<1 \text{ g cm}^{-2} \text{ ka}^{-1}$), altered biogeochemical cycling

61 and increased transportation of water vapor to North America [Haug et al., 1999; Sigman et al.,
62 2004; Haug et al., 2005; Swann et al., 2006; Reynolds et al., 2008; Shimada et al., 2009; Swann
63 2010; Bailey et al., 2011; Studer et al., 2012].

64 In contrast to ODP Site 882, records at Site U1341 in the Bering Sea remain stable and
65 show no collapse in siliceous productivity at 2.73 Ma and over the onset of NHG [Iwasaki et al.,
66 2016]. Instead, fluxes of both biogenic opal (from c. 2-4 g cm⁻² ka⁻¹ to c. 8-12 g cm⁻² ka⁻¹) and
67 organic carbon (from < 0.1 mol C m⁻² y⁻¹ to c. 0.3 mol C m⁻² y⁻¹) increase abruptly later at 2.58
68 Ma [März et al., 2013; Wehrmann et al., 2013; Iwasaki et al., 2016]. Two alternative
69 explanations exist that link the increase in siliceous productivity at Site U1341 from 2.58 Ma to
70 oceanographic changes in the subarctic North Pacific Ocean. Stratification and associated
71 reductions in productivity and nutrient utilization at ODP Site 882 [Haug et al., 1999; Sigman et
72 al., 2004; Reynolds et al., 2008; Bailey et al., 2011] could have led to the export of nutrient-rich
73 deep/intermediate waters that were upwelled at Bowers Ridge to fuel the productivity increase at
74 Site U1341 [März et al., 2013]. This mechanism is consistent with evidence for a global change
75 in patterns of opal sedimentation, nutrient availability and the efficiency of the biological pump
76 at the Pliocene/Quaternary boundary [Cortese et al., 2004; Etourneau et al., 2012], but does not
77 account for the time lag between the establishment of the halocline at ODP Site 882 (2.73 Ma)
78 and the increase in opal at U1341 (2.58 Ma). An alternative hypothesis, building on the status of
79 the Bering Sea as a HNLC region, links the high opal MAR from 2.58 Ma to iron fertilization
80 from the Bering Sea continental shelf [Iwasaki et al., 2016].

81 Diatom silicon isotope ($\delta^{30}\text{Si}_{\text{diatom}}$) measurements are presented from Site U1341,
82 between 2.93-2.52 Ma, in order to better constrain changes in biogeochemical cycling in the
83 south Bering Sea and to obtain insights into how the region responded to the abrupt
84 reorganization of the subarctic northwest Pacific Ocean at 2.73 Ma. Silicon, in the form of silicic
85 acid [Si(OH)₄] is a key nutrient for diatoms. During the biomineralisation of silicic acid into
86 particulate hydrous silica the lighter ²⁸Si isotope is preferentially taken up by diatoms over the
87 heavier stable isotopes ²⁹Si and ³⁰Si, with an enrichment factor (ϵ) of -1.1‰ to -1.2‰ that is
88 independent of temperature, *p*CO_{2(aq)}, iron availability and other vital effects [De La Rocha et
89 al., 1997; Milligan et al., 2004; Varela et al., 2004; Fripiat et al., 2011]. With progressive uptake
90 of Si(OH)₄ increasing the $\delta^{30}\text{Si}$ (³⁰Si/²⁸Si) of Si(OH)₄ remaining in the water column via
91 Rayleigh distillation, values of $\delta^{30}\text{Si}_{\text{diatom}}$ reflect changes in the rate of silicic acid [Si(OH)₄]
92 utilization and/or supply of Si(OH)₄ to the photic zone [De La Rocha, 2006; Hendry and
93 Brzezinski, 2014]. Accordingly, records of $\delta^{30}\text{Si}_{\text{diatom}}$ can be used to constrain the alternative
94 mechanisms that initiated the opal increase at U1341 from 2.58 Ma onwards. A nutrient leakage
95 from the subarctic North Pacific Ocean would be expected to increase the supply of Si(OH)₄ to
96 the photic zone at Site U1341. Changes in Si(OH)₄ utilization may also occur under this
97 scenario, depending on the net efficiency of the biological pump. In contrast, iron fertilization
98 should only lead to a change in rate of Si(OH)₄ utilization at Site U1341, due to the resultant
99 reduction in diatom frustule Si:N uptake ratios [Hutchins and Bruland, 1998; Takeda, 1998].
100 Diatom silica oxygen isotope measurements ($\delta^{18}\text{O}_{\text{diatom}}$) reflect surface water temperature and
101 salinity conditions [Swann and Leng, 2009] and are also presented between 2.93-2.52 Ma in
102 order to provide information on the wider surface ocean environment.

103 **2 Methods**104 **2.1 Age models**

105 The age model for Site U1341 is taken from Iwasaki et al. [2016] in which linear
106 sedimentation rates are applied between 13 age control point based on shipboard paleomagnetic
107 measurements and refined biostratigraphy [Expedition 323 Scientists, 2011; Takahashi et al.,
108 2011; Onodera et al., 2016; Ikenoue et al., 2016]. The sedimentation rates, age controls points
109 and respective errors for the interval analyzed in this study [reported in Table 1 of Iwasaki et al.,
110 2016] are shown in Figure 2. Whilst the ages of some control points are well established (e.g.,
111 top of Gauss at 2.581 Ma) the biostratigraphic datums have uncertainties of up to 0.08 Ma. To
112 address this overlap of datum events within their uncertainties, the average depths of datum
113 events were used to establish ages at 2.48 and 2.65 Ma [see full details in Iwasaki et al., 2016].
114 The impact of age model uncertainties on the linear sedimentation rates and the increase in opal
115 MAR at 2.6 Ma are fully discussed in Iwasaki et al. [2016]. Whilst Iwasaki et al. [2016]
116 acknowledge that uncertainties in the age model may impact the absolute opal MAR values, they
117 remain confident that the increase in opal MAR represents a marked increase in biological
118 productivity rather than an age-model artefact.

119 **2.2 Diatom isotopes**

120 Seventy samples from Site U1341B (54°1.9984'N, 179°0.5171'E; water depth = 2,140 m)
121 on Bowers Ridge in the south Bering Sea, dated between 2.93-2.52 Ma, were prepared for
122 diatom isotope analysis using a combination of heavy liquid separation and reagents to remove
123 contaminants [Swann et al., 2013]. Samples were sieved at 38 μm , 15 μm and at 3 μm using a
124 sieve cloth to isolate diatoms from sponge spicules that reflect bottom water conditions and
125 possess different fractionation factors to diatoms [de la Rocha, 2003; Wille et al., 2010; Hendry
126 and Robinson, 2012; Snelling et al., 2014]. Sample size fractions were screened using a Zeiss
127 Axiovert 40 C inverted microscope, scanning electron microscope (SEM) and X-ray
128 fluorescence (XRF) to confirm sample purity and the absence of non-diatom contaminants; the
129 cleanest size fraction was retained for isotope analysis. Out of the seventy samples, 68 were
130 analyzed for $\delta^{18}\text{O}_{\text{diatom}}$ and 24 for $\delta^{30}\text{Si}_{\text{diatom}}$. Of the 68 samples analyzed for $\delta^{18}\text{O}_{\text{diatom}}$, 26 were
131 from the >38 μm fraction and 42 from the 3-15 μm fraction. Previous research found a
132 significant offset between different diatom size fractions analyzed for $\delta^{18}\text{O}_{\text{diatom}}$ [Swann et al.,
133 2007, 2008]. However, comparison of 18 pairs of 3-15 μm and >38 μm size fraction samples at
134 Site U1341, selected from throughout the analyzed interval, reveals no offset beyond analytical
135 reproducibility. Diatoms in the >38 μm size fraction are dominated by *Actinocyclus curvatulus*,
136 *Coscinodiscus marginatus* and *Shionodiscus trifultus*. The 3-15 μm size fraction is composed of
137 a variety of taxa including *Neodenticula seminae* and *Neodenticula koizumii* together with
138 fragments from larger taxa. Given the diversity of taxa in the analyzed samples, our isotope
139 records are interpreted as recording mean annual conditions with a significant bias towards
140 spring months when productivity peaks [Rho and Whitledge, 2007; Brown et al., 2011; Sigler et
141 al., 2014].

142 Samples were analyzed for $\delta^{18}\text{O}_{\text{diatom}}$ and $\delta^{30}\text{Si}_{\text{diatom}}$ using a combined step-wise
143 fluorination procedure at the NERC Isotope Geosciences Facility based at the British Geological
144 Survey [Leng and Sloane, 2008]. $\delta^{18}\text{O}_{\text{diatom}}$ and $\delta^{30}\text{Si}_{\text{diatom}}$ were measured on a Finnigan MAT
145 253 with results converted to the Vienna Standard Mean Ocean Water (VSMOW) and NBS28

146 scale, respectively, using the within-run laboratory diatom standard BFC_{mod} which has been
 147 calibrated against NBS28. These methods have been verified through inter-laboratory calibration
 148 exercises for both $\delta^{18}\text{O}_{\text{diatom}}$ [Chapligin et al., 2011] and $\delta^{30}\text{Si}_{\text{diatom}}$ [Reynolds et al., 2007].
 149 Replicate analyses of sample material across the interval analyzed from Site U1341 indicate an
 150 analytical reproducibility (1σ) of 0.4‰ and 0.09‰ for $\delta^{18}\text{O}_{\text{diatom}}$ and $\delta^{30}\text{Si}_{\text{diatom}}$, respectively.

151 2.3 Silicic acid utilization/supply

152 The isotope fractionation of silicon during biological uptake can be considered within the
 153 context of either a closed or open system model under Rayleigh fractionation. In a closed system
 154 model all $\text{Si}(\text{OH})_4$ is supplied to the photic zone prior to biological uptake. In open ocean
 155 systems, such as the region around Site U1341, silicon dynamics are best represented by an open
 156 system model marked by continuous supply of silicic acid to the photic zone. In this, through
 157 Rayleigh distillation, changes in $\delta^{30}\text{Si}_{\text{diatom}}$ are a function of the isotopic composition of the
 158 dissolved silicic acid [$\delta^{30}\text{Si}(\text{OH})_4$] supplied to the photic zone, the fraction of $\text{Si}(\text{OH})_4$ remaining
 159 in the water (f) and the enrichment factor between diatoms and dissolved silicic acid (ϵ):

$$160 \quad \delta^{30}\text{Si}_{\text{diatom}} = \delta^{30}\text{Si}(\text{OH})_4 + \epsilon * f$$

161 (Eq. 1)

162 No investigation into the contemporary $\delta^{30}\text{Si}$ systematics of the Bering Sea has been
 163 undertaken. Research in the subarctic North Pacific Ocean has measured $\delta^{30}\text{Si}(\text{OH})_4$ at $1.23 \pm$
 164 0.17‰ (2σ ; water depth = 10 m at “Station 3”: $50^{\circ}00'\text{N}$, $167^{\circ}00'\text{E}$) and ϵ as -1.0 [Reynolds et
 165 al., 2006] and we use these values for the Bering Sea. Using these modern values and
 166 extrapolating to the Pliocene/early Quaternary introduces a degree of uncertainty into the
 167 quantitative estimates of $\text{Si}(\text{OH})_4$ utilization/supply calculated from Equations 2 and 3 below.
 168 However, the use of subarctic North Pacific Ocean end-members from a site close to ODP Site
 169 882 is appropriate when testing whether nutrient leakage from the region caused the increase in
 170 opal MAR at Site U1341 at 2.58 Ma. Using the modern values, Equation 1 can be re-written to
 171 calculate changes in $\text{Si}(\text{OH})_4$ utilization [% $\text{Si}(\text{OH})_4$ utilization]:

$$172 \quad \% \text{Si}(\text{OH})_4 \text{ utilization} = 1 - \frac{\delta^{30}\text{Si}_{\text{diatom}} - 1.23}{-1.0}$$

173 (Eq. 2)

174 Following Horn et al. (2011) changes in $\text{Si}(\text{OH})_4$ utilization between 2.93-2.52 Ma can
 175 then be combined with interpolated estimates of opal MAR [Iwasaki et al., 2016] to constrain
 176 temporal changes in the relative supply of $\text{Si}(\text{OH})_4$ [% $\text{Si}(\text{OH})_4$ supply] into the photic zone
 177 relative to the youngest sample at 2.52 Ma:

$$178 \quad \% \text{Si}(\text{OH})_4 \text{ supply} = \frac{\text{Opal}_{\text{sample}} / \text{Opal}_{2.52 \text{ Ma}}}{\% \text{Si}(\text{OH})_4 \text{ utilization-sample} / (\% \text{Si}(\text{OH})_4 \text{ utilization-2.52 Ma})}$$

179 (Eq. 3)

180 where $\text{Opal}_{\text{sample}}$ and $\% \text{Si}(\text{OH})_4 \text{ utilization-sample}$ are the opal MAR and rate of $\text{Si}(\text{OH})_4$
 181 utilization for a given sample respectively and where $\text{Opal}_{2.52 \text{ Ma}}$ and $\% \text{Si}(\text{OH})_4 \text{ utilization-2.52 Ma}$ are
 182 the opal MAR and magnitude of $\text{Si}(\text{OH})_4$ utilization in our youngest sample at 2.52 Ma. This

183 approach assumes that the degree of biogenic silica dissolution through the water column and
184 within the sediment record has remained unchanged over the analyzed interval.

185 **3 Results**

186 **3.1 $\delta^{30}\text{Si}_{\text{diatom}}$**

187 $\delta^{30}\text{Si}_{\text{diatom}}$ does not show a large change at Site U1341 over the onset of major NHG (Fig.
188 2). Between 2.93-2.52 Ma values of $\delta^{30}\text{Si}_{\text{diatom}}$ generally vary between 0.9‰ and 1.2‰ (\bar{x} =
189 1.0‰, 1σ = ± 0.2 ‰) with variations in $\delta^{30}\text{Si}_{\text{diatom}}$ from 2.73-2.58 Ma similar to the preceding 200
190 ka. No clear link exists between changes in $\delta^{30}\text{Si}_{\text{diatom}}$ and glacial/interglacial cycles, although the
191 resolution of the $\delta^{30}\text{Si}_{\text{diatom}}$ record is too low to fully investigate this (Fig. 2). Exceptions to these
192 relatively stable $\delta^{30}\text{Si}_{\text{diatom}}$ values occur in the oldest sample at 2.93 Ma (0.48‰) and from 2.58
193 Ma onwards when values range from 0.50‰ (2.55 Ma) to 1.36‰ (2.53 Ma) (Fig. 2). Estimates
194 of $\text{Si}(\text{OH})_4$ utilization follow the patterns in $\delta^{30}\text{Si}_{\text{diatom}}$ and show that the low values of $\delta^{30}\text{Si}_{\text{diatom}}$
195 at 2.93 Ma and 2.55 Ma are associated with reduced levels of nutrient utilization (Fig. 2). Rates
196 of $\text{Si}(\text{OH})_4$ supply to the photic zone were c. 50%, relative to the youngest sample at 2.52 Ma,
197 prior to the onset of major NHG at 2.73 Ma (\bar{x} = 49‰, 1σ = ± 8 ‰) when excluding the
198 exceptionally high value of 219% at 2.93 Ma (Fig. 2). After 2.73 Ma rates of supply
199 progressively increased to c. 65% at 2.60 Ma (\bar{x} = 59‰, 1σ = ± 8 ‰). From 2.58 Ma onwards,
200 coinciding with increases in opal MAR [Iwasaki et al., 2016], $\text{Si}(\text{OH})_4$ supply to the photic zone
201 abruptly increases to 81-397% for the remainder of the analyzed interval (Fig. 2) (\bar{x} = 154‰, 1σ
202 = 113‰).

203 **3.2 $\delta^{18}\text{O}_{\text{diatom}}$**

204 Through the late Pliocene $\delta^{18}\text{O}_{\text{diatom}}$ is relatively stable from 2.82-2.93 Ma (\bar{x} = 39.8‰,
205 1σ = ± 0.4 ‰) (Fig. 2). In the build up to the intensification of NHG (2.73 Ma) and until 2.63 Ma
206 values of $\delta^{18}\text{O}_{\text{diatom}}$ increase and oscillate over a magnitude of 3.0‰ (\bar{x} = 40.7‰, 1σ = ± 0.9 ‰).
207 After 2.63 Ma and until 2.58 Ma $\delta^{18}\text{O}_{\text{diatom}}$ becomes more stable, displaying a long term increase
208 to values of c. 42‰. After 2.58 Ma until the end of the analyzed interval at 2.52 Ma $\delta^{18}\text{O}_{\text{diatom}}$
209 remains both high and relatively stable (\bar{x} = 41.6‰, 1σ = ± 0.5 ‰) (Fig. 2).

210 **4 Discussion**

211 **4.1 Nutrient leakage v iron fertilization**

212 Two hypotheses exist to explain the opal MAR increase at 2.58 Ma in the south Bering
213 Sea: (1) iron fertilization [Iwasaki et al., 2016]; and (2) nutrient leakage from the North Pacific
214 Ocean [März et al., 2013]. The lack of a concordant change in rates of $\text{Si}(\text{OH})_4$ utilization and
215 opal MAR at 2.58 Ma would appear to rule out iron fertilization given that the addition of iron to
216 a HNLC region should alter diatom frustule silicon uptake [Hutchins and Bruland, 1998; Takeda,
217 1998], although not all studies document a clear relationship between iron fertilization and
218 diatom elemental ratios [e.g., Hoffmann et al., 2007]. The increase in opal MAR and rates of
219 $\text{Si}(\text{OH})_4$ supply at 2.58 Ma instead supports the concept of a silicic acid/nutrient leakage fueling
220 the bloom via inflow from the subarctic North Pacific Ocean through the Kamchatka Strait and
221 potentially the Near Strait [März et al., 2013]. Whilst the Kamchatka Strait is a location of
222 significant outflow from the Bering Sea, inflow of $\text{Si}(\text{OH})_4$ rich subarctic Pacific waters occurs

223 on the eastern side of the strait and at depths [Reed et al., 1993; Cokelet et al., 1996; Coachman
224 et al., 1999; Stabeno et al., 1999] (Fig. 1b).

225 Si(OH)_4 leakage from the subarctic North West Pacific Ocean, linked to the decline in
226 opal MAR and halocline formation at ODP Site 882, would have commenced from 2.73 Ma.
227 However, the opal MAR increase at Site U1341 begins later at 2.58 Ma. The $\delta^{30}\text{Si}_{\text{diatom}}$ data from
228 Site U1341 provide an important insight to this time lag by demonstrating that the rate of
229 Si(OH)_4 supply to the Bering Sea increased gradually, not abruptly, following the formation of
230 the subarctic North Pacific Ocean halocline at 2.73 Ma through to the opal MAR increase at 2.58
231 Ma (Fig. 3). Changes in sea level, for which no data exist, could be responsible for this by
232 regulating flow through the Kamchatka Strait and potentially the Near Strait (Fig. 1).
233 Alternatively, the long-term increase in Si(OH)_4 supply to Site U1341 may reflect a progressive
234 increase in the intensity of nutrient leakage from the subarctic Pacific over the same interval.

235 At ODP Site 882, the decrease in opal MAR and development of the halocline leads to
236 anti-correlated records of $\delta^{30}\text{Si}_{\text{diatom}}$ and nitrogen isotopes ($\delta^{15}\text{N}$) measured on bulk sediment and
237 on diatoms [Reynolds et al., 2008; Bailey et al., 2011; Studer et al., 2012] (Fig. 3). Using
238 Equations 2/3 and subarctic North Pacific Ocean values for $\delta^{30}\text{Si(OH)}_4$ and ϵ of 1.23‰ and 1.0
239 respectively [Reynolds et al., 2006], we calculate rates of Si(OH)_4 utilization for ODP Site 882
240 (Fig. 3). Rather than remaining stable, rates of Si(OH)_4 utilization at ODP Site 882 show a long-
241 term shift to lower values after 2.73 Ma (Fig. 3). This trend could be related to increases in
242 dust/iron deposition [Bailey et al., 2011] and indicates a gradually more under-utilized pool of
243 Si(OH)_4 in the subarctic Pacific Ocean after 2.73 Ma. Consequently, subarctic North Pacific
244 waters exported through the Kamchatka Strait into the Bering Sea would have become
245 progressively more enriched in Si(OH)_4 between 2.73 Ma and 2.58 Ma, leading to the observed
246 pattern of higher rates of Si(OH)_4 supply to Site U1341 over the same interval (Fig. 3).

247 **4.2 Opal productivity increase from 2.58 Ma**

248 Both Si(OH)_4 supply and opal MAR at Site U1341 increase abruptly from 2.58 Ma
249 onwards, indicating a major change in the regional water column structure. Prior to 3.1 Ma the
250 region around Bowers Ridge was characterized by relatively warm waters both at Site U1340
251 and U1341 [Chen et al., 2014; Zhang et al., 2014; Stroynowski et al., 2015] (Fig. 1). Thereafter,
252 and in particular with the onset of major NHG, diatom and radiolarian assemblages indicate a
253 gradual cooling that accelerated with the emergence of low-salinity surface waters related to the
254 expansion of sea ice [Chen et al., 2014; Zhang et al., 2014; Stroynowski et al., 2015]. Values of
255 $\delta^{18}\text{O}_{\text{diatom}}$ at Site U1341 differ considerably from those reported at ODP Site 882 in terms of the
256 magnitude and timing of isotope changes [Haug et al., 2005; Swann et al., 2006; Swann, 2010],
257 reflecting differences in temperature, glacial meltwater and precipitation inputs at each site. At
258 Site U1341 the onset of major NHG is associated with a shift in $\delta^{18}\text{O}_{\text{diatom}}$ to more variable
259 values including frequent increases to 41–42‰, indicative of the emergence of colder surface
260 water conditions (Fig. 2). No clear link exists between $\delta^{18}\text{O}_{\text{diatom}}$ and rates of Si(OH)_4
261 supply/opal MAR at U1341 prior to 2.58 Ma. However, the increase in siliceous productivity
262 after 2.58 Ma coincides with the stabilization of $\delta^{18}\text{O}_{\text{diatom}}$ at high values (c. 42‰) (Fig. 2). This
263 change, advocating the transition to persistent colder surface waters, is concordant with increases
264 in the relative abundance of the diatoms *Neodenticula koizumii* and *Actinocyclus curvatulus*,
265 interpreted as indicating a decrease in sea surface temperatures [Onodera et al., 2016].

266 Phytoplankton dynamics in the Bering Sea are primarily regulated by a combination of
267 winter winds, mixing the water column and supplying nutrients to the photic zone, and seasonal
268 stratification, either linked to spring sea ice melt and/or seasonal increases in solar insolation
269 [Katsuki and Takahashi, 2005]. We propose that the transition to persistent cold conditions at
270 2.58 Ma, as indicated by $\delta^{18}\text{O}_{\text{diatom}}$, is linked to enhanced wind-driven mixing at Site U1341 that
271 significantly increased the advection of cold, $\text{Si}(\text{OH})_4$ -rich, deep water exported from the
272 subarctic North Pacific Ocean to the surface at Bowers Ridge. This explains the abrupt increase
273 in $\text{Si}(\text{OH})_4$ supply at 2.58 Ma and does not necessitate an abrupt increase in nutrient leakage
274 through the Kamchatka Strait at 2.58 Ma. An increase in wind-driven mixing could be linked to
275 either regional changes in the Aleutian storm track and/or global changes in storm/cyclone
276 frequency and sea-surface temperature gradients [Fedorov et al., 2013; 2015]. In addition, a shift
277 to a more productive environment would also be supported by the observed increases in regional
278 sea ice from c. 2.65-2.60 Ma onwards [Onodera et al., 2016; Stroynowski et al., 2015]. Whilst
279 Site U1341 lies south of the current sea ice, expansion of sea ice beyond the Bering shelf break
280 has also been documented in late Quaternary glacial periods [Katsuki and Takahashi, 2005;
281 Caissie et al., 2010].

282 In summary, the combination of increases in wind-driven mixing, sea ice-driven
283 stratification and photic zone $\text{Si}(\text{OH})_4$ supply at 2.58 Ma would have created oceanographic
284 conditions similar to those found along the Bering Shelf today, in which phytoplankton blooms
285 are aided by sea ice melt that creates a seasonally stratified system which entrains diatoms in the
286 photic zone [Aguilar-Islas et al., 2007; Ladd and Stabeno, 2012; Brown and Arrigo, 2013]. This
287 interpretation is supported by both diatom assemblages, indicating nutrient-depleted stratified
288 surface waters in summer months following the main diatom bloom [Stroynowski et al., 2015],
289 and slightly higher levels of $\text{Si}(\text{OH})_4$ utilization in 4 of the 6 samples analyzed post 2.58 Ma
290 (Fig. 2). The highly variable rates of $\text{Si}(\text{OH})_4$ utilization and $\text{Si}(\text{OH})_4$ supply from 2.58-2.52 Ma,
291 however, advocates the need for further work on this interval and may reflect short-term changes
292 in either sea-ice abundance, wind-driven advection and/or nutrient leakage to the Bering Sea
293 (Fig. 2).

294 **5 Conclusions**

295 Diatom isotope records from Site U1341 in the south Bering Sea show that the onset of
296 major NHG from c. 2.73 Ma coincided with a series of changes that culminated in an abrupt
297 increase in siliceous productivity at 2.58 Ma. Between 2.73 Ma and 2.58 Ma rates of $\text{Si}(\text{OH})_4$
298 supply to the photic zone gradually increased, attributed to nutrient leakage from the subarctic
299 northwest Pacific Ocean where a corresponding decline in $\text{Si}(\text{OH})_4$ utilization is apparent over
300 the same period. At the same time $\delta^{18}\text{O}_{\text{diatom}}$ indicates a variable, but progressive, shift to colder
301 conditions. These changes end after 2.58 Ma with an abrupt increase in $\text{Si}(\text{OH})_4$ supply to the
302 photic zone, fueling the observed increase in opal concentrations. With $\delta^{18}\text{O}_{\text{diatom}}$ suggesting a
303 shift to persistently colder conditions from 2.58 Ma, increased $\text{Si}(\text{OH})_4$ supply from the deep to
304 surface waters at Site U1341 could be linked to increased wind-driven mixing of the water
305 column. In any case, increased $\text{Si}(\text{OH})_4$ availability in the photic zone, combined with
306 microfossil evidence for increased sea ice and a seasonally stratified water column, would have
307 created optimal conditions for high levels of siliceous productivity. Further research is now
308 needed to assess the long-term impact of this nutrient leakage from the subarctic Northwest
309 Pacific Ocean to the Bering Sea. Did this leakage culminate in the early Quaternary, or did
310 nutrient leakage from the subarctic Pacific continue to play a key role in Bering Sea

311 biogeochemical cycling through the Quaternary - for example over glacial-interglacial cycles in
312 line with documented shifts between intervals of higher (interglacial) and lower (glacial)
313 productivity [Katsuki and Takahashi 2005; Iwasaki et al., 2016]?

314 **Acknowledgments and Data**

315 Supporting data ($\delta^{18}\text{O}_{\text{diatom}}$ and $\delta^{30}\text{Si}_{\text{diatom}}$ data from Site U1341 between 2.93 Ma and 2.52 Ma)
316 are included as a spreadsheet in the SI. This work was funded through Natural Environment
317 Research Council (NERC) grant NE/I005889/1. Thanks are owed to Hilary Sloane [NIGL/BGS]
318 for assistance with the sample analysis, Sev Kender [University of Nottingham] for commenting
319 on an earlier version of the manuscript and to Christian März, an anonymous reviewer and the
320 editorial team at *Paleoceanography* for their constructive comments.

321 **References**

- 322 Aguilar-Islas, A. M., M. P. Hurst, K. N. Buck, B. Sohst, G. J. Smith, M. C. Lohan, and K.W.
323 Bruland (2007), Micro- and macronutrients in the southeastern Bering Sea: Insight into
324 iron-replete and iron-depleted regimes, *Prog Oceanogr.*, 73, 99-126.
- 325 Bailey, I., Q. Liu, G. E. A. Swann, Z. Jiang, Y. Sun, X. Zhao, and A. P. Roberts, A.P. (2011),
326 Iron fertilisation and biogeochemical cycles in the sub-Arctic northwest Pacific during
327 the late Pliocene intensification of northern hemisphere glaciation, *Earth Planet Sc Lett.*,
328 307, 253-265.
- 329 Brown, Z. W., and K. R. Arrigo (2013), Sea ice impacts on spring bloom dynamics and net
330 primary production in the Eastern Bering Sea, *J Geophys Res.*, 118, 43-63.
- 331 Brown, Z. W., G. L van Dijken, and K. R. Arrigo (2011), A reassessment of primary production
332 and environmental change in the Bering Sea, *J Geophys Res.*, 116, C08014,
333 doi:10.1029/2010JC006766.
- 334 Caissie, B. E., J. Brigham-Grette, K. T. Lawrence, T. D. Herbert, and M. S. Cook (2010), Last
335 Glacial Maximum to Holocene sea surface conditions at Umnak Plateau, Bering Sea, as
336 inferred from diatom, alkenone, and stable isotope records, *Paleoceanography*, 25,
337 PA1206, doi:10.1029/2008PA001671.
- 338 Chaplignin, B., M. Leng, E. Webb, A. Alexandre, J. Dodd, A. Ijiri, A. Lucke, A. Shemesh, A.
339 Abelman-Gersonde, U. Herzschuh, F. Longstaffe, H. Meyer, R. Moschen, Y. Okazaki,
340 N. Rees, Z. Sharp, H. Sloane, C. Sonzogni, G. Swann, F. Sylvestre, J. Tyler, and R. Yam
341 (2011), Inter-laboratory comparison of oxygen isotope compositions from biogenic silica,
342 *Geochim. Cosmochim. Ac.*, 75, 7242–7256.
- 343 Chen, M. -H., Q. Zhang, L. -L. Zhang, C. Alvarez Zarikian and R. -J. Wang (2014), Stratigraphic
344 distribution of the radiolarian *Spongodiscus biconcavus* Haeckel at IODP Site U1340 in
345 the Bering Sea and its paleoceanographic significance. *Palaeoworld* 23, 90-104.
- 346 Coachman, L. K., T. E. Whitledge, and J. J. Goering (1999), in T. R. Loughlin and K. Ohtani,
347 eds., *Dynamics of the Bering Sea: Fairbanks*, University of Alaska Sea Grant Press, AK-
348 SG-99-03, 285-310.
- 349 Cokelet, E. D., M. L. Schall, and D. M. Dougherty, D.M (1996), ADCP- referenced geostrophic
350 circulation in the Bering Sea, *J Phys Oceanogr.*, 26, 1113-1128.

- 351 Cortese, G., R. Gersonde, C. -D. Hillenbrand, and G. Kuhn (2004), Opal sedimentation shifts in
352 the World Ocean over the last 15 Myr, *Earth Planet Sc Lett.*, 224, 509-527.
- 353 de La Rocha, C.L., M. A. Brzezinski, and M. J. DeNiro (1997), Fractionation of silicon isotopes
354 by marine diatoms during biogenic silica formation, *Geochim. Cosmochim. Ac.* 61,
355 5051-5056.
- 356 de la Rocha, C. L. (2003), Silicon isotope fractionation by marine sponges and the reconstruction
357 of the silicon isotope composition of ancient deep water, *Geology*, 31, 423-426.
- 358 de da Rocha, C. L. (2006), Opal-based isotopic proxies of paleoenvironmental conditions, *Global*
359 *Biogeochem Cy.*, 20, GB4S09, doi:10.1029/2005GB002664.
- 360 Etourneau, J., C. Ehlert, M. Frank, P. Martinez, and R. Schneider (2012), Contribution of
361 changes in opal productivity and nutrient distribution in the coastal upwelling systems to
362 Late Pliocene/Early Pleistocene climate cooling, *Clim Past.*, 8, 1435-1445.
- 363 Expedition 323 Scientists (2011), Site U1341. In Takahashi, Ravelo, A.C., K., Alvarez Zarikian,
364 C.A., and the Expedition 323 Scientists, *Proc. IODP, 323: Tokyo (Integrated Ocean*
365 *Drilling Program Management International, Inc.)*. doi:10.2204/iodp.proc.323.105.2011.
- 366 Fedorov, A. V., C. M. Brierley, K. T. Lawrence, Z. Liu, P. S. Dekens, and A. C. Ravelo (2013),
367 Patterns and mechanisms of early Pliocene warmth, *Nature*, 496, 43-48.
- 368 Fedorov, A. V., N. J. Burls, K. T. Lawrence, and L. C. Peterson (2015), Tightly linked zonal and
369 meridional sea surface temperature gradients over the past five million years, *Nat Geosci*,
370 8, 975-980.
- 371 Fripiat, F., A. -J. Cavagna, F. Dehairs, S. Speich, L. André, and D. Cardinal (2011), Silicon pool
372 dynamics and biogenic silica export in the Southern Ocean inferred from Si-isotopes,
373 *Ocean Sci.*, 7, 533-547.
- 374 Haug, G. H., D. M. Sigman, R. Tiedemann, T. F. Pedersen, and M. Sarnthein (1999), Onset of
375 permanent stratification in the subarctic Pacific Ocean, *Nature*, 401, 779-782.
- 376 Haug, G. H., A. Ganopolski, D. M. Sigman, A. Rosell-Mele, G. E. A. Swann, R. Tiedemann, S.
377 Jaccard, J. Bollmann, M. A. Maslin, M. J. Leng, and G. Eglinton (2005), North Pacific
378 seasonality and the glaciation of North America 2.7 million years ago, *Nature*, 433, 821-
379 825.
- 380 Hendry, K. R., and L. F. Robinson (2012), The relationship between silicon isotope fractionation
381 in sponges and silicic acid concentration: Modern and core-top studies of biogenic opal,
382 *Geochim. Cosmochim. Ac.*, 81, 1-12.
- 383 Hendry, K. R., and M. A. Brzezinski (2014), Using silicon isotopes to understand the role of the
384 Southern Ocean in modern and ancient biogeochemistry and climate, *Quaternary Science*
385 *Reviews*, 89, 13-26.
- 386 Hidy, A. J., J. C. Gosse, D. G. Froese, J. D. Bond, and D. H. Rood (2013), A latest Pliocene age
387 for the earliest and most extensive Cordilleran Ice Sheet in northwestern Canada,
388 *Quaternary Sci Rev.*, 61, 77-84.

- 389 Hoffmann, L. J., I. Peeken, and K. Lochte (2007), Effects of iron on the elemental stoichiometry
390 during EIFEX and in the diatoms *Fragilariopsis kerguelensis* and *Chaetoceros dichaeta*,
391 *Biogeosciences*, 4, 569-579.
- 392 Horn, M. G., C. P. Beucher, R. S. Robinson, and M. A. Brzezinski (2011), Southern ocean
393 nitrogen and silicon dynamics during the last deglaciation, *Earth and Planet Sc Lett.* 310,
394 334-339.
- 395 Hutchins, D. A., and K. W. Bruland (1998), Iron-limited diatom growth and Si:N uptake ratios in
396 a coastal upwelling regime, *Nature*, 393, 561-564.
- 397 Ikenoue, T., Y. Okazaki, Z. Takahashi, and T. Sakamoto (2016), Bering Sea radiolarian
398 biostratigraphy and paleoceanography at IODP Site U1341 during the last four million
399 years, *Deep-Sea Res Pt II.*, 125-126, 38-55.
- 400 Iwasaki, S., K. Takahashi, Y. Kanematsu, H. Asahi, J. Onodera, and A. C. Ravelo (2016),
401 Paleoproductivity and paleoceanography of the last 4.3 Myrs at IODP Expedition 323
402 Site U1341 in the Bering Sea based on biogenic opal content, *Deep-Sea Res Pt II.*, 125-
403 126, 145-154.
- 404 Katsuki, K., and K. Takahashi (2005) Diatoms as paleoenvironmental proxies for seasonal
405 productivity, sea-ice and surface circulation in the Bering Sea during the late Quaternary,
406 *Deep-Sea Res Pt II.*, 52, 2110-2130.
- 407 Kinney, J. C., and W. Maslowski (2012), On the oceanic communication between the Western
408 Subarctic Gyre and the deep Bering Sea, *Deep-Sea Res Pt I.*, 66, 11-25.
- 409 Ladd, C., and P. J. Stabeno (2012), Stratification on the Eastern Bering Sea shelf revisited, *Deep-
410 Sea Res Pt II.*, 65-70, 72-83.
- 411 Leng, M. J., and H. J. Sloane (2008), Combined oxygen and silicon isotope analysis of biogenic
412 silica, *J Quaternary Sci.*, 23, 313-319.
- 413 März, C., B. Schnetger, and H. -J. Brumsack (2013), Nutrient leakage from the North Pacific to
414 the Bering Sea (IODP Site U1341) following the onset of Northern Hemispheric
415 Glaciation?, *Paleoceanography*, 28, 68-78.
- 416 Maslin, M. A., G. H. Haug, M. Sarnthein, and R. Tiedemann (1996), The progressive
417 intensification of northern hemisphere glaciation as seen from the North Pacific, *Geol
418 Rundsch.*, 85, 452-465.
- 419 Milligan, A. J., D. E. Varela, M. A. Brzezinski, and F. O. M. M. Morel (2004), Dynamics of
420 silicon metabolism and silicon isotopic discrimination in a marine diatom as a function of
421 $p\text{CO}_2$, *Limnol. Oceanogr.* 49, 322-329.
- 422 Mudelsee, M., and M. E. Raymo (2005), Slow dynamics of the Northern Hemisphere glaciation,
423 *Paleoceanography*, 20, PA4022, doi:10.1029/2005PA001153.
- 424 Onodera, J., K. Takahashi, and R. Nagatomo (2016), Diatoms, silicoflagellates, and ebridians at
425 Site U1341 on the western slope of Bowers Ridge, IODP Expedition 323, *Deep-Sea Res
426 Pt II.*, 125-126, 8-17.
- 427 Ravelo, A. C., D. H. Andreasen, M. Lyle, A. O. Lyle, and M. W. Wara (2004), Regional climate
428 shifts caused by gradual global cooling in the Pliocene epoch, *Nature*, 429, 263-267.

- 429 Raymo, M. E. (1994), The Himalayas, organic carbon burial, and climate in the Miocene,
430 *Paleoceanography*, 9, 399-404.
- 431 Reed, R. K., G. V. Khen, P. J. Stabeno, and A. V. Verkhunov (1993), Water properties and flow
432 over the deep Bering Sea basin, summer 1991, *Deep-Sea Res Pt I.*, 40, 2325-2334.
- 433 Reynolds, B. C., M. Frank, and A. N. Halliday (2006), Silicon isotope fractionation during
434 nutrient utilization in the North Pacific, *Earth Planet Sc Lett.*, 244, 431-443.
- 435 Reynolds, B. C., J. Aggarwal, L. André, D. Baxter, C. Beucher, M. A. Brzezinski, E. Engström,
436 R. B. Georg, M. Land, M. J. Leng, S. Opfergelt, I. Rodushkin, H. J. Sloane, S. H. J. M.
437 van den Boorn, P. Z. Vroom, and D. Cardinal (2007), An inter-laboratory comparison of
438 Si isotope reference materials, *J Anal Atom Spectrom.*, 22, 561-568.
- 439 Reynolds, B. C., M Frank, and A. N. Halliday (2008), Evidence for a major change in silicon
440 cycling in the subarctic North Pacific at 2.73 Ma, *Paleoceanography* 23, PA4219,
441 doi:10.1029/2007PA001563.
- 442 Rho, T., and T. E. Whitley (2007), Characteristics of seasonal and spatial variations of primary
443 production over the southeastern Bering Sea shelf, *Cont Shelf Res.*, 27, 2556-2569.
- 444 Sambrotto, R. N., J. J. Goering, and C. P. McRoy (1984), Large Yearly Production of
445 Phytoplankton in the Western Bering Strait, *Science*, 225, 1147-1150.
- 446 Shimada, C., T. Sato, M. Yamasaki, S. Hasegawa, and Y. Tanaka (2009) Drastic change in the
447 late Pliocene subarctic Pacific diatom community associated with the onset of the
448 Northern Hemisphere Glaciation, *Palaeogeogr Palaeocl.*, 279, 207-215.
- 449 Sigler, M. F., P. J. Stabeno, L. B. Eisner, J. M. Napp, and F. J. Mueter (2014), Spring and fall
450 phytoplankton blooms in a productive subarctic ecosystem, the eastern Bering Sea,
451 during 1995–2011, *Deep-Sea Res Pt II.*, 109, 71-83.
- 452 Sigman, D. M., S. L. Jaccard, and G. H. Haug (2004) Polar ocean stratification in a cold climate,
453 *Nature*, 428, 59-63.
- 454 Snelling, A. M., G. E. A. Swann, J. Pike, and M. J. Leng (2014) Pliocene diatom and sponge
455 spicule oxygen isotope ratios from the Bering Sea: isotopic offsets and future directions,
456 *Clim Past.*, 10, 1837-1842
- 457 Stabeno, P. J., J. D. Schumacher, and K. Ohtani (1999), Physical oceanography of the Bering
458 Sea. In: *The Bering Sea: a Summary of Physical, Chemical and Biological Characteristics*
459 *and a Synopsis of Research*. T. R. Loughlin, and K. Ohtani (ed). North Pacific Marine
460 Science Organization, PICES, Alaska Sea Grant Press, pp. 1-28.
- 461 Stroynowski, Z., and A. C. Ravelo, and D. Andreasen (2015), A Pliocene to recent history of the
462 Bering Sea at Site U1340A, IODP Expedition 323, *Paleoceanography*, 30, 1641-1656.
- 463 Studer, A. S., A. Martínez-García, S. L. Jaccard, F. E. Girault, D. M. Sigman, and G. H. Haug
464 (2012), Enhanced stratification and seasonality in the Subarctic Pacific upon Northern
465 Hemisphere Glaciation—New evidence from diatom-bound nitrogen isotopes, alkenones
466 and archaeal tetraethers, *Earth Planet Sc Lett.*, 351-352, 84-94.

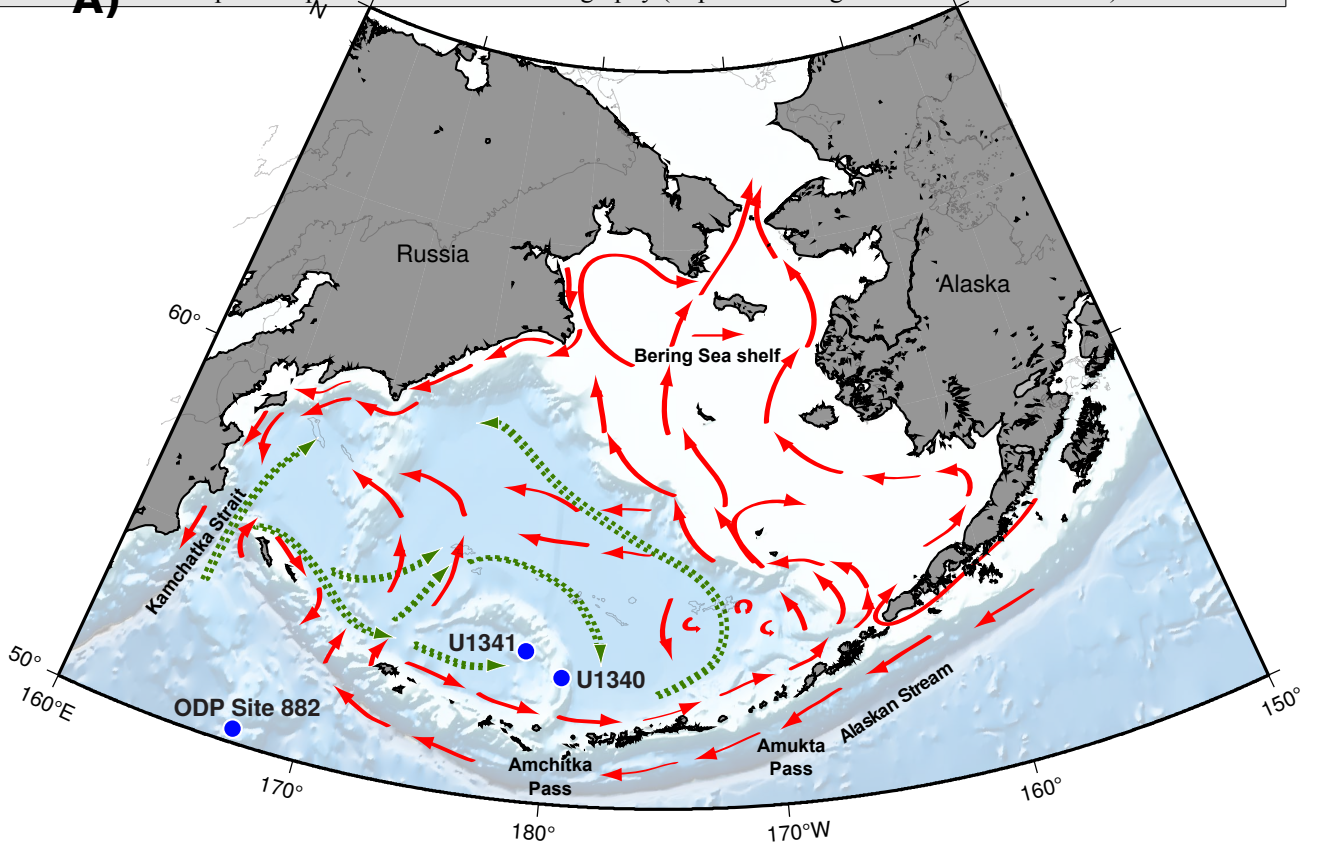
- 467 Swann, G. E. A. (2010), Salinity changes in the North West Pacific Ocean during the late
468 Pliocene/early Quaternary from 2.73 Ma to 2.53 Ma, *Earth Planet Sc Lett.*, 297, 332-338,
469 2010.
- 470 Swann, G. E. A., and M. J. Leng (2009) A review of diatom $\delta^{18}\text{O}$ in palaeoceanography,
471 *Quaternary Sci Rev.*, 28, 384-398.
- 472 Swann, G. E. A., M. A. Maslin, M. J. Leng, H. J. Sloane, and G. H. Haug (2006), Diatom $\delta^{18}\text{O}$
473 evidence for the development of the modern halocline system in the subarctic northwest
474 Pacific at the onset of major Northern Hemisphere glaciation, *Paleoceanography*, 21,
475 PA1009, doi:10.1029/2005PA001147.
- 476 Swann, G. E. A., M. J. Leng, H. J. Sloane, M. A. Maslin, and J. Onodera (2007), Diatom oxygen
477 isotopes: evidence of a species effect in the sediment record. *Geochem Geophys Geosy.*,
478 8, Q06012, doi:10.1029/2006GC001535.
- 479 Swann, G. E. A., M. J. Leng, H. J. Sloane, and M. A. Maslin, M. A (2008), Isotope offsets in
480 marine diatom $\delta^{18}\text{O}$ over the last 200 ka, *J Quaternary Sci.*, 23, 389-400.
- 481 Swann, G. E. A., J. Pike, A. M. Snelling, M. J. Leng, and M. C. Williams (2013), Seasonally
482 resolved diatom $\delta^{18}\text{O}$ records from the west Antarctic Peninsula over the last
483 deglaciation, *Earth Planet Sc Lett.*, 364, 12-23.
- 484 Takahashi, K. (2005), The Bering Sea and paleoceanography, *Deep-Sea Res Pt II.*, 52, 2080-
485 2091.
- 486 Takahashi, K., A. C. Ravelo, and C. A. Alvarez Zarikian, Expedition 323 Scientists (2011) In:
487 *Proceedings of the Integrated Ocean Drilling Program 323: Integrated Ocean Drilling*
488 *Program Management International, Inc., Tokyo.*
- 489 Takeda, S. (1998), Influence of iron availability on nutrient consumption ratio of diatoms in
490 oceanic waters, *Nature*, 393, 774-777.
- 491 Tiedemann, R., and G. H. Haug (1995), Astronomical calibration of cycle stratigraphy for site
492 882 in the northwest Pacific, *Proc. Ocean Drill. Program Sci. Results*, 145, 283 – 292.
- 493 Varela, D. E., C. J. Pride, and M. A. Brzezinski (2004), Biological fractionation of silicon
494 isotopes in Southern Ocean surface waters, *Global Biogeochem. Cy.*, 18,
495 doi:10.1029/2003GB002140.
- 496 Wehrmann, L. M., S. Arndt, C. März, T. G. Ferdelman, and B. Brunner (2013), The evolution of
497 early diagenetic signals in Bering Sea seafloor sediments in response to varying
498 organic carbon deposition over the last 4.3 Ma, *Geochim. Cosmochim. Ac.*, 109, 175-
499 196.
- 500 Wille, M., J. Sutton, M. J. Ellwood, M. Sambridge, W. Maher, S. Eggins, and M. Kelly (2010),
501 Silicon isotopic fractionation in marine sponges: A new model for understanding silicon
502 isotopic variations in sponges, *Earth Planet Sc Lett.*, 292, 281-289.
- 503 Zhang, Q., M. Chen, L. Zhang, W. Hu, and R. Xiang (2014), Variations in the radiolarian
504 assemblages in the Bering Sea since Pliocene and their implications for
505 paleoceanography, *Palaeogeogr Palaeoclimatol.*, 410, 337-350.

507 **Figures**

508 **Figure 1:** a) Map showing location of Hole U1341B at IODP Site 1341 (54°1.9984'N,
509 179°0.5171'E) and Hole U1340A at IODP Site 1340 (53°24.0008'N, 179°31.2973'W) on Bowers
510 Ridge in the Bering Sea and ODP Site 882 in the subarctic North West Pacific Ocean
511 (50°21.797'N, 167°35.999'E) together with surface (red lines) and subsurface (dashed green
512 lines) water circulation in the Bering Sea [adapted from Stabeno et al., 1999; Takahashi et al.,
513 2011]. b) Cross sections of the passes and volume transport (S_v) in the Aleutian Island [adapted
514 from Stabeno et al., 1999; Takahashi, 2005; Takahashi et al., 2011].

515 **Figure 2:** $\delta^{18}\text{O}_{\text{diatom}}$ and $\delta^{30}\text{Si}_{\text{diatom}}$ at Site U1341 together with calculated estimates of $\text{Si}(\text{OH})_4$
516 utilization, $\text{Si}(\text{OH})_4$ supply and opal MAR [Iwasaki et al., 2016]. Rates of $\text{Si}(\text{OH})_4$ supply are
517 relative to a value of 100% in the uppermost sample at 2.52 Ma and, for clarity, the y-axis on the
518 plot is log transformed. Vertical dashed lines indicate onset of major NHG (2.73) and the opal
519 MAR increase at Site U1341 at 2.58 Ma. Sedimentation rates (gray line) and age control points
520 (coloured triangles) are from Table 1 in Iwasaki et al. [2016]. Blue and red dashed lines for the
521 control points at 2.64 Ma and 2.65 Ma are the age errors also reported within Table 1 in Iwasaki
522 et al. [2016].

523 **Figure 3:** Comparison of $\delta^{30}\text{Si}_{\text{diatom}}$ and $\text{Si}(\text{OH})_4$ utilization at ODP Site 882 (Fig. 1) in the
524 subarctic Northwest Pacific Ocean with $\text{Si}(\text{OH})_4$ supply and opal MAR [Iwasaki et al., 2016] at
525 Site U1341 in the Bering Sea. For clarity the y-axis on the $\text{Si}(\text{OH})_4$ supply data plot from Site
526 U1341 is log transformed. Vertical dashed lines indicate onset of major NHG (2.73) and the opal
527 MAR increase at Site U1341 at 2.58 Ma. The age model for ODP Site 882 is based on the linear
528 interpolation of sedimentation rates between tie-points derived from the astronomical calibrated
529 of high resolution GRAPE density and magnetic susceptibility measurements [Tiedemann and
530 Haug, 1995].

A)Accepted for publication in *Paleoceanography* (<http://dx.doi.org/10.1002/2016PA002978>)**B)**